Boron anomaly in the thermal conductivity of lithium borate glasses

Sørensen, Søren Strandskov; Johra, Hicham; Mauro, John C.; Bauchy, Mathieu; Smedskjær, Morten Mattrup

Published in:
Physical Review Materials

DOI (link to publication from Publisher):
10.1103/PhysRevMaterials.3.075601

Publication date:
2019

Document Version
Publisher's PDF, also known as Version of record

Boron anomaly in the thermal conductivity of lithium borate glasses

Søren S. Sørensen,[1] Hicham Johra,[2] John C. Mauro,[3] Mathieu Bauchy,[4] and Morten M. Smedskjaer[1,*]
[1]*Department of Chemistry and Bioscience, Aalborg University, Aalborg, Denmark*
[2]*Department of Civil Engineering, Aalborg University, Aalborg, Denmark*
[3]*Department of Materials Science and Engineering, The Pennsylvania State University, University Park, Pennsylvania 16802, USA*
[4]*Department of Civil and Environmental Engineering, University of California, Los Angeles, California 90095, USA*

(Received 1 April 2019; published 1 July 2019)

Despite the importance of thermal conductivity for a range of modern glass applications, its compositional dependence and structural origins in modified oxide glasses remain poorly understood. In particular, the thermal conductivity of oxide glasses with network formers other than silica remain almost unexplored and no thorough connection with structural characteristics of glasses has been made. In this work, we study the thermal conductivity of binary lithium borate glasses using both experiments and classical molecular dynamics (MD) simulations. This glass system is chosen due to the nonmonotonic evolution in the boron coordination number as a function of composition and because glasses may be made in a wide compositional window. Specifically, we show that thermal conductivity exhibits a clear boron anomaly effect, as observed in both experiments and MD simulations. Thermal conduction is thus believed to mainly be promoted by the presence of fourfold coordinated boron. However, simulated vibrational density of states for the studied series suggests that the thermal conductivity is also influenced by the presence of the modifier ions based on an observed overlap between Li and O modes. Overall these results provide insights into the connection between thermal conductivity and structure of modified oxide glasses, which is the first step toward developing a model for predicting the composition dependence of thermal conductivity.

DOI: 10.1103/PhysRevMaterials.3.075601

I. INTRODUCTION

The thermal conductivity of oxide glasses has not been well studied in the literature, although it is an important property for a number of applications, e.g., the performance of insulation materials and coatings in microelectronics [1,2]. In addition, there could be potentially exciting applications for new glass compositions featuring either very high or low values of thermal conductivity [1]. The heat transfer mechanisms in noncrystalline systems are in general poorly understood. Simple additive, empirical models for the composition dependence of thermal conductivity in bulk oxide glasses have been proposed, but they cannot capture variations across different glass families due to the lack of physical insights [3,4]. The phonon gas model (PGM), which treats transport of phonons as quasiparticles that can be modeled like gas molecules, has been successfully used to understand heat conduction in crystalline solids [5]. However, recent studies suggest that it often fails to describe heat conduction in glasses and amorphous solids, although it remains an important tool for understanding the behavior of propagating modes [5–11]. Modern computational methods have improved the understanding of heat propagation in noncrystalline materials [7,12,13], but the structural origins of the composition dependence of thermal conductivity, especially in modified oxide glasses, remain unclear.

Various experimental studies have been published on the thermal conductivity of oxide glasses with a variety of motivations and approaches, including low-temperature studies to understand the boson peak and an observed thermal conductivity plateau [14,15], high-temperature studies to understand melt-dynamics [4,16,17], and room temperature studies focusing on a specific application [3,18–21]. The vast majority of published studies focus on silica-based glasses, with the general observation that an increasing fraction of network modifiers leads to a decrease in the thermal conductivity due to the depolymerization of the rigid network [3,4,22]. Besides SiO_2, B_2O_3 is another common network former that is a major component in a variety of industrial glasses [23]. Glassy B_2O_3 consists of corner-sharing BO_3 triangles (B^3), a large fraction of which combine to form three-membered boroxol ring units [24]. Network modifier addition (e.g., alkali oxide) either leads to charge-stabilization of fourfold coordinated boron (B^4), which increases the connectivity of the network, or creation of a nonbridging oxygen, thereby rupturing the linkage between two trigonally coordinated B^3 groups [25].

The literature on thermal conductivity in borate-based glasses is, however, sparse. A study by Ghoneim and Halawa concludes that the thermal conductivity of a series of sodium borosilicate glasses at room temperature does not exhibit the well-known boron anomaly, i.e., there is no nonmonotonic composition dependence of thermal conductivity due to the change in boron coordination number [19]. On the other hand, more recent studies by Kim *et al.* show a nonlinearity in the thermal conductivity in the molten state for a series of sodium borates in the

*Corresponding author: mos@bio.aau.dk

TABLE I. Analyzed compositions, density (ρ), glass transition temperature (T_g), fraction of fourfold coordinated to total boron (N_4), longitudinal sound velocity (v_L), transversal sound velocity (v_T), Debye sound velocity (v_D), isobaric heat capacity extrapolated to 300 K (C_p), thermal diffusivity (α), and thermal conductivity (κ) at 300 K for the experimentally prepared glasses. Average estimated errors for ρ, T_g, α, and κ are $\pm 0.003\,\mathrm{g\,cm^{-3}}$, $\pm 2\,\mathrm{K}$, $0.003\,\mathrm{mm^2\,s^{-1}}$, and $0.007\,\mathrm{W\,m^{-1}\,K^{-1}}$, respectively.

ID	$[Li_2O]$ (mol%)	$[B_2O_3]$ (mol%)	ρ ($\mathrm{g\,cm^{-3}}$)	T_g (°C)	N_4[a] (%)	v_L[b] ($\mathrm{m\,s^{-1}}$)	v_T[b] ($\mathrm{m\,s^{-1}}$)	v_D ($\mathrm{m\,s^{-1}}$)	C_p ($\mathrm{J\,g^{-1}\,K^{-1}}$)	α ($\mathrm{mm^2\,s^{-1}}$)	κ ($\mathrm{W\,m^{-1}\,K^{-1}}$)
Li0	0	100	1.823	248	0	3500	2004	2227	0.873	0.315	0.502
Li10	9.6	90.4	1.987	349	11.2	4672	2750	3048	0.881	0.369	0.643
Li15	14.6	85.4	2.056	405	17.7	5329	2943	3279	0.934	0.379	0.728
Li20	19.9	80.1	2.121	462	25.0	5814	3267	3635	0.938	0.389	0.775
Li25	24.7	75.3	2.195	493	32.9	6217	3544	3939	0.977	0.407	0.870
Li30	29.5	70.5	2.245	499	39.7	6607	3752	4171	1.000	0.423	0.951
Li35	34.5	65.5	2.279	492	42.9	6880	3946	4383	1.036	0.419	0.990
Li40	39.9	60.1	2.289	472	43.4	7008	4028	4474	1.082	0.410	1.015
Li48	47.7	52.3	2.256	440	38.4	–	–	–	1.137	0.388	0.996

[a]Data extrapolated from Reference [25].
[b]Data extrapolated from Reference [58].

concentration range of 0–30 mol% Na_2O [26]. The same authors later observed a similar nonlinearity in molten potassium borates, suggesting a correlation between thermal conductivity and the boron coordination change from B^3 to B^4 as determined by Raman spectroscopy. However, molten lithium borates exhibit only a slight deviation from linearity in the range of 10–30 mol% Li_2O [27,28]. Furthermore, these studies only included three compositions of each series, making it challenging to evaluate the possible boron anomaly effect in thermal conductivity for these systems. To our knowledge, the only published work on thermal conductivity of alkali borates in the glassy state is that of Tohmori *et al.*, which studied a series of seven sodium borate glasses in the composition range of 5–35 mol % Na_2O [29]. They reported a monotonic increase of thermal conductivity with increasing fraction of Na_2O.

In this study, we investigate the thermal diffusivity and conductivity in a series of nine lithium borate glasses with Li_2O contents from 0 to 48 mol%. Our aim is to understand the structural origin of the observed trend in thermal conductivity in the glassy state. The lithium borate system was chosen due to its wide glass-forming window [30,31] and the presence of the boron anomaly in various properties such as glass transition temperature and density [31–33]. To gain additional structural information about the heat conduction processes, we compare the experimental results with simulations of thermal conductivity through the Green-Kubo (GK) approach using molecular dynamics (MD). This is possible given the recent advances in developing empirical potentials for boron-containing glasses [34,35]. Here, we apply the potential developed by Deng and Du [34], as it is also parametrized for lithium. Only few comparisons between experimental and simulated values of thermal conductivity in oxide glasses have been made, focusing mostly on pure SiO_2 [36,37]. Indeed, to our knowledge, no MD simulations of the thermal conductivity in modified borate glasses have been reported. This study thus serves as an attempt at correlating structure of modified oxide glasses with thermal conductivity. Such understanding is needed in various systems to achieve our ultimate goal of developing a quantitative model for predicting the thermal conductivity in oxide glasses.

II. EXPERIMENTAL METHODS

A. Sample preparation

We prepared glasses in the $x$$Li_2O$-(100-$x$)$B_2O_3$ series (in mol%) with $x = 0$, 10, 15, 20, 25, 30, 35, 40, and 48. This was done by first mixing Li_2CO_3 (Merck, $\geqslant$98.5%) and H_3BO_3 (Fluka, $\geqslant$99.5%) in appropriate amounts, followed by melting at 950–1050 °C for 1 h in Pt-Rh crucibles. All melts were quenched onto a brass plate and then annealed for ~30 min at their estimated glass transition temperature (T_g) based on literature data [31]. Some compositions had to be pressed by another metal plate upon quenching to ensure more rapid cooling and thus avoid crystallization. The compositions of the samples were determined by inductively coupled plasma optical emission spectroscopy (ICP-OES) measurements (Table I). Only glass samples without visual crystallization were used for further analysis. For the three compositions with greatest tendency to crystallize ($x = 30,\ 35,$ and 40), we performed x-ray diffraction (PANalytical Empyrean) analysis on powdered samples, confirming that they are x-ray amorphous (see Fig. S1 in the Supplemental Material [38]). All samples were stored in desiccators to limit hydration.

B. Characterization

To confirm proper annealing of the glasses, we measured their T_g values using differential scanning calorimetry (DSC, Netzsch 449F1). This was done on samples that were cut and polished in ethanol into cylinders of ~6-mm diameter and ~1-mm height. These were then heated to above their glass transition range followed by a cooling at 10 $\mathrm{K\,min^{-1}}$ to at least 100 °C below T_g and a subsequent heating to above the T_g at 10 $\mathrm{K\,min^{-1}}$ [39]. The T_g values reported in Table I correspond to the onset temperature of the calorimetric glass transition peak. We determined the isobaric heat capacity (C_p) as a function of temperature using a sapphire standard. In order to convert thermal diffusivity (see below) to thermal conductivity, we need to know C_p at room temperature. This value was obtained by extrapolating the C_p data to 27 °C (300 K) using the Maier-Kelley equation [40],

$$C_p(T) = a + bT - cT^{-2}, \quad (1)$$

TABLE II. Number of atoms, density (ρ_{MD}), fraction of fourfold coordinated to total boron ($N_{4,MD}$), longitudinal sound velocity ($v_{L,MD}$), transversal sound velocity ($v_{T,MD}$), Debye sound velocity ($v_{D,MD}$), and thermal conductivity (κ_{MD}) for the simulated glasses. All values are recorded at 300 K, except for the $v_{l,MD}$, $v_{T,MD}$, and $v_{D,MD}$, which have been estimated at 0 K. Average errors for $N_{4,MD}$, $v_{L,MD}$, $v_{T,MD}$, $v_{D,MD}$, and κ_{MD} are 0.3%, 18 m s^{-1}, 30 m s^{-1}, 31 m s^{-1}, and 0.097 W m^{-1} K^{-1}, respectively.

ID	#Li atoms	#B atoms	#O atoms	ρ_{MD} (g cm^{-3})	$N_{4,MD}$ (%)	$v_{L,MD}$ (m s^{-1})	$v_{T,MD}$ (m s^{-1})	$v_{D,MD}$ (m s^{-1})	κ_{MD} (W m^{-1} K^{-1})
MD0	0	1200	1800	1.934	0	4418	2106	2369	2.404
MD10	125	1125	1750	1.984	3.1	5517	2982	3328	2.662
MD15	191	1085	1724	2.036	9.2	6115	3317	3701	2.773
MD20	261	1043	1696	2.077	16.4	6913	3795	4231	2.774
MD25	333	1000	1667	2.136	29.4	7388	4354	4825	2.885
MD30	409	955	1636	2.182	40.4	7684	4571	5061	3.055
MD35	488	907	1605	2.205	47.5	7800	4673	5170	3.085
MD40	571	857	1572	2.206	48.2	7804	4656	5151	2.863
MD45	659	805	1536	2.221	44.3	7776	4725	5221	2.753
MD50	750	750	1500	2.169	31.2	7238	4371	4832	2.590

where T is temperature and a, b, and c are empirical fitting parameters. The model was fitted to C_p data from around 150 to around 30 °C below T_g for each composition by using a least squares method. An example of the fit is shown in Fig. S2 in the Supplemental Material [38].

Density (ρ) of the annealed glasses was determined using Archimedes' principle of buoyancy with ethanol at 22.6 °C. All samples used for density determination had masses larger than 0.75 g and the mass measurements were repeated ten times.

Thermal diffusivity (α) was measured using laser flash analysis (LFA) (Netzsch LFA 447). For this analysis, the samples were cut into cylinders with diameter of either 12.7 or 10.0 mm and thickness in the range of ∼1–2 mm. These were polished to an optical finish in ethanol and found to be coplanar within ±10 μm. Prior to the measurements, the samples were coated with a thin layer of graphite to ensure optimum laser pulse absorption, good thermal thermal response of the infrared (IR) sensor of the instrument, and to decrease initial spikes in the recorded signal due to the sample transparency. The samples were irradiated with a Xe-laser and the temperature increase was recorded by an IR detector on the opposite side. This temperature profile was then fitted to a model in the Netzsch Proteus® LFA analysis software in order to calculate the thermal diffusivity (α). The model used for the LFA includes both radiation and pulse correction. The diffusivity data were measured at 300 K. Subsequently the thermal conductivity (κ) was calculated from the measured heat capacity and density,

$$\kappa = \rho C_p \alpha. \tag{2}$$

III. COMPUTATIONAL METHODS

A. Glass preparation

Ten glasses in the xLi$_2$O-(100-x)B$_2$O$_3$ series (see Table II) were simulated by classical MD simulations in LAMMPS [41]. This was done using a combination of the Coulomb and Buckingham potentials, as well as a spline of the potential at low separation values to avoid the Buckingham catastrophe. We apply the parameters and the quenching procedure from the work of Deng and Du [34]. An interaction cutoff of 11 Å was used for the short range interactions, while Coulombic interactions were treated as long range forces and computed directly below 11 Å and using the PPPM method above 11 Å. A timestep of 1 fs was used for all simulation steps. First, 3000 atoms were placed randomly in a box of ∼5% lower density than the experimental value (Table I). This was followed by energy minimization and equilibration of the system at 300 K for 60 ps in the *NVT* ensemble. Next the temperature was raised to 6000 K and the system was allowed to randomize for 100 ps in the *NVT* ensemble to lose the memory of its initial configuration. The system was then cooled instantenously to 5000 K, where it was equilibrated for another 100 ps in the *NVT* ensemble, before the system was quenched from 5000 to 300 K at 5 K ps^{-1} in the *NVT* ensemble. After the quench, the system was allowed to relax at 300 K for 60 ps at zero pressure in the *NPT* ensemble, before a final 60 ps of relaxation in the *NVT* ensemble.

B. Structural characterization

To evaluate the ability of the potential to predict a realistic glass structure, we compute the neutron total radial distribution function (RDF) as a weighed sum of the partial RDFs,

$$g_N(r) = \left(\sum_{i,j=1}^{n} c_i c_j b_i b_j \right)^{-1} \sum_{i,j=1}^{n} c_i c_j b_i b_j g_{ij}(r), \tag{3}$$

where c_i is the fraction of atoms i, b_i is the neutron scattering length of atom type i (−1.9, 6.65, and 5.803 fm for lithium, boron-11, and oxygen, respectively), and $g_{ij}(r)$ is the partial RDF of the atom pair i,j. Simulated total RDFs were broadened by convoluting the total RDF with a Gaussian distribution with a full width at half maximum (FWHM) of,

$$\mathrm{FWHM} = \frac{5.437}{Q_{max}}, \tag{4}$$

where Q_{max} is the experimental maximum wave vector. In this study, we use $Q_{max} = 40$ Å^{-1} because this was reported as

the maximum Q value in the experimental neutron diffraction data [42].

Structure factor comparisons were made by first calculating the partial structures factors as

$$S_{ij}(Q) = 1 + \rho_a \int_0^{r_{\max}} 4\pi r^2 (g_{ij}(r) - 1) \frac{\sin(Qr)}{Qr} \frac{\sin\left(\frac{\pi r}{r_{\max}}\right)}{\frac{\pi r}{r_{\max}}} dr, \tag{5}$$

where Q is the wave vector, ρ_a is the average atom number density, $r_{\max}$ is the maximum radius for the integration (here half the simulation box size because of the use of periodic boundary conditions). The $\sin(\pi r/r_{\max})/(\pi r/r_{\max})$ part is a Lorch type function used to reduce ripples of the Fourier transform due to the finite cutoff of r. The total total neutron structure factor was then calculated from the partial structure factors,

$$S_{\mathrm{N}}(Q) = \left(\sum_{i,j=1}^{n} c_i c_j b_i b_j \right)^{-1} \sum_{i,j=1}^{n} c_i c_j b_i b_j S_{ij}(Q). \tag{6}$$

The boron coordination number distribution was evaluated by counting the number of neighbors of each atom within the first coordination shell (by using a 2 Å cutoff). This evaluation is used to discriminate between three- and fourfold coordinated boron. All structural parameters are presented as averages of ten structures from the final *NVT* relaxation.

C. Thermal conductivity

We compute the thermal conductivity based on the GK method, as it has proven successful for a wide variety of systems with both low and high values of κ. Moreover, it is not directly dependent on the system size contrary to nonequilibrium methods, for which it can be challenging to extrapolate to bulk values of κ [43,44]. Following the GK approach,

$$\kappa = \frac{V}{3k_{\mathrm{B}}T^2} \int_0^{\infty} \langle \mathbf{J}(0) \cdot \mathbf{J}(t) \rangle dt, \tag{7}$$

where V is the volume of the simulation box, k_{B} is Boltzmann's constant, T is temperature, t is time, and $\langle \mathbf{J}(0) \cdot \mathbf{J}(t) \rangle$ is the heat current autocorrelation function (HCACF). Naturally, it is impossible to simulate to infinite time and practically we thus record the HCACF until it converges to zero.

First the temperature of the as-prepared glass was set to 300 K in the *NVE* ensemble and the structure was further relaxed for 10 ps. This was followed by averaging over 2000 HCACFs, each of 5 ps, giving a total simulation time for data collection of 10 ns. For each composition, we performed ten measurements of κ with different random velocity profiles of the systems. The results are given as $\kappa_{\mathrm{mean}} \pm \sigma N^{-1/2}$ [45], where κ_{mean} is the average thermal conductivity of the ten simulations, σ is the standard deviation, and N is the number of simulations. An example of a simulated, normalized HCACF is shown in Fig. S3 in the Supplemental Material [38].

D. Sound velocity

The speed of sound is used in several models of thermal conductivity, including the phonon gas model. To determine it herein by MD, the prepared glasses were first quenched from 300 to 0 K at 1 K ps^{-1} in the *NPT* ensemble at zero pressure, before performing an energy minimization of the obtained structure. Hereafter stress-strain curves were obtained by deforming the simulation box with a given strain, followed by minimization to get the stress in the deformed direction. The obtained stress-strain curves were used to obtain the stiffness matrix elements. Based on the assumed isotropic nature of the glasses, C_{11} was computed as the average of C_{11}, C_{22}, and C_{33}, while C_{44} was computed as the average of C_{44}, C_{55}, and C_{66}. The obtained values were used to evaluate the longitudinal and transversal sound velocity [46],

$$v_{\mathrm{L}} = \sqrt{\frac{C_{11}}{\rho_{\mathrm{MD}}}}, \tag{8}$$

$$v_{\mathrm{T}} = \sqrt{\frac{C_{44}}{\rho_{\mathrm{MD}}}}, \tag{9}$$

where ρ_{MD} is the simulated density value.

E. Vibrational density of states and modal contribution to heat current

To obtain some insights into the heat propagation mechanism, we evaluate the vibrational density of states (VDOS, $g(\omega)$) of each simulated glass,

$$g(\omega) = \sum_{j}^{n} m_j c_j \int_0^{\infty} \langle \mathbf{v}_j(0) \cdot \mathbf{v}_j(t) \rangle e^{i\omega t} dt, \tag{10}$$

where m_j is the mass of atom type j, c_j is the fraction of atom type j, $\langle \mathbf{v}_j(0) \cdot \mathbf{v}_j(t) \rangle$ is the average of the velocity autocorrelation function (VACF) of atom type j, ω is the frequency, and t is time. In practice, 100 VACFs, each of 2 ps, were collected for each atom type and the presented VDOS is an average over these.

To study the qualitative contribution of modes to the measured heat current, we apply the Fourier transform to the HCACF [47,48],

$$\kappa(\omega) = \int_0^{\infty} \langle \mathbf{J}(0) \cdot \mathbf{J}(t) \rangle e^{i\omega t} dt, \tag{11}$$

which enables qualitative inspection of the contribution of each mode to the HCACF. In turn, this allows us to distinguish between contributing and noncontributing modes to the heat flux and thus thermal conductivity.

IV. RESULTS AND DISCUSSION

A. Structural characterization

Figure 1 shows a comparison of the neutron structure factor obtained from the present simulations and experiments from literature [42]. Data are here shown for pure B_2O_3 and $20Li_2O$-$80B_2O_3$ glasses, while a comparison for two additional glasses in the series are shown in Fig. S4 in the Supplemental Material [38]. For the B_2O_3 glass (MD0), we observe a good agreement between simulations and experiments for Q values above 5 Å^{-1}, with some minor deviations noticed below 5 Å^{-1}, especially for the positions of

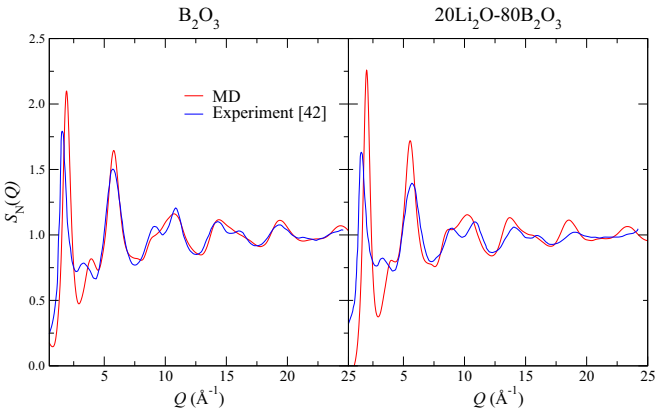

FIG. 1. Comparison of simulated and experimental neutron structure factors $S_N(Q)$ for two glass compositions. Experimental structure factors are from Ref. [42].

the first and second diffraction peaks. Considering that Q values translate into the inverse distance in real space, this means that the short-range order (SRO) is well captured by the potential, while the medium-range order (MRO) is less well described. Analysis of the ring size distributions in the MD0 glass (see naming in Table II) shows that only rings larger than the typical boroxol ring exist, which may, at least partially, explain the structural deviation in the MRO [49,50]. For the MD20 glass, the agreement with experiments is worse compared to the results for MD0, which is also the case for the other two compositions shown in Fig. S4 in the Supplemental Material [38]. Again, we observe deviations in the peak positions for Q values below 5 Å^{-1}, but for this composition, deviation is also present at Q values above 20 Å^{-1}. Nonetheless, the potential generally reproduces the peak positions in the medium Q ranges, whereas deviations in the peak intensities are observed.

To study the SRO in more detail, we compare the neutron radial distribution functions, $g_N(r)$, of the MD0 and MD20 glasses in Fig. 2 [42]. Again, for the MD0 glass, good agreement is seen between simulation and experimental data. The

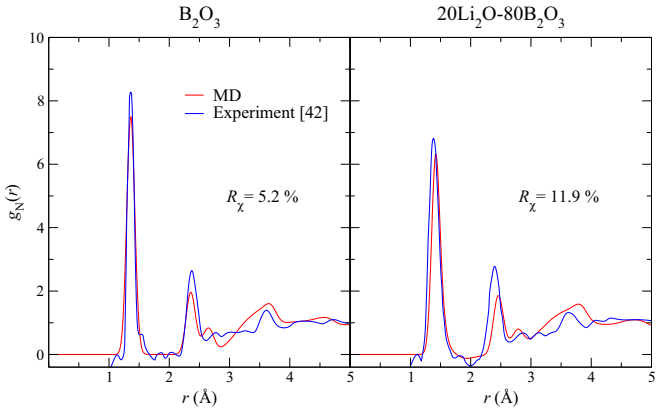

FIG. 2. Comparison of simulated and experimental radial distribution function $g_N(r)$ for two glass compositions. Experimental data are from Ref. [42]. Simulated $g_N(r)$ are broadened following the approach by Wright [51] using $Q_{max} = 40$ Å^{-1}.

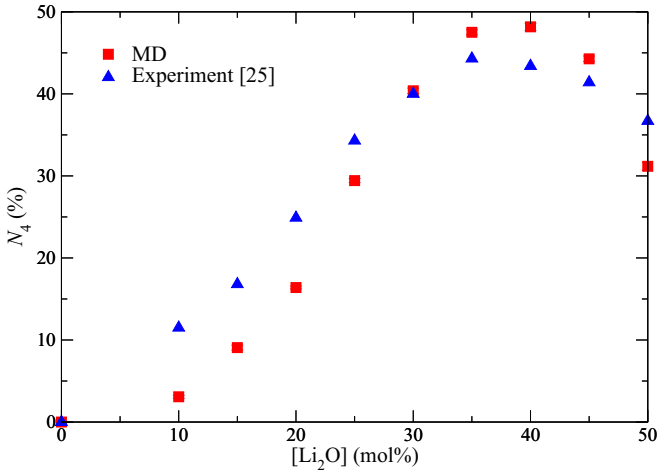

FIG. 3. Composition dependence of the fraction of fourfold coordinated to total boron (N_4) in the lithium borate glasses. N_4 is obtained both experimentally (in Ref. [25]) and from the present MD simulations. Error bars for MD data are all smaller than the size of the symbols.

first major diffraction peak is well produced, but the minor shoulder at ∼1.5 Å is not reproduced by the potential. The remaining part of the structure is described qualitatively well by the potential, with some deviation in the peak intensities. We note that the negative peak around 2 Å is due to the negative neutron scattering length of lithium. Using the R_χ metric introduced by Wright to quantitatively evaluate the agreement between experiments and simulations, we obtain $R_\chi = 5.2\%$, where $R_\chi < 9\%$ is generally considered to be in good agreement [51]. For the MD20 glass, the first peak is reproduced in intensity, yet nearly all peaks seem to be shifted to slightly higher r values and peaks of higher r values also seem to deviate in intensity. The latter was also noted by the deviation in the SRO part of the structure factor (Fig. 1). For this glass, we obtain $R_\chi = 11.9\%$, suggesting that the potential does not capture the full structural details, although the main peaks are qualitatively well reproduced. Deviations in peak positions are the main cause of the high R_χ value.

To further evaluate the validity of the potential, we consider an important structural descriptor for borate glasses, that is, the fraction of fourfold coordinated to total boron (N_4). The nonmonotonic composition dependence of N_4 is the typical descriptor used to account for the structural origin of the boron anomaly effect in properties such as the density and thermal expansion coefficient [33,52]. Figure 3 shows a comparison of the composition dependence of N_4 for both the present simulations and experimental data from Ref. [25]. The compositional trend in N_4 is well captured by the MD simulations, namely, the increasing fraction of fourfold coordinated boron with increasing lithium modifier content as well as the decrease in N_4 above ∼40 mol% Li_2O. We note that this is expected considering that the utilized MD potential has been parametrized to match the N_4 values of the model by Dell, Bray, and Xiao [34,53]. Although the qualitative trend is captured, we also note that the simulations slightly underestimate the absolute values of N_4 at low Li_2O contents. At higher lithium concentration, even the absolute

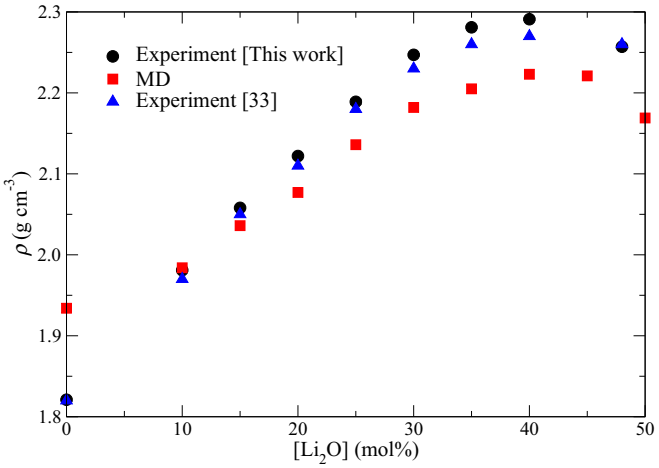

FIG. 4. Composition dependence of the density (ρ) in the lithium borate glasses as obtained from experiments (present study and Ref. [33]) and MD simulations. Error bars of experiments are smaller than the size of the symbols.

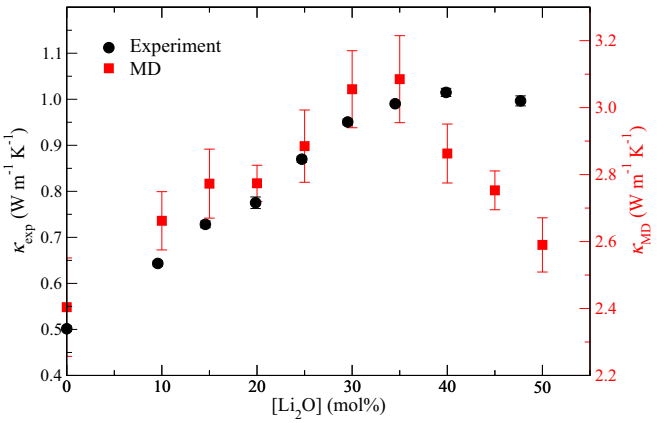

FIG. 5. Composition dependence of the thermal conductivity (κ) at 300 K in the lithium borate glasses as obtained from both experiments and MD simulations as a function of Li_2O content. The error bars of the experimental κ are generally smaller than the size of the symbols.

values show good agreement with experiments, including the maximum in N_4. As such, the utilized pair potential is able to structurally reproduce the boron anomaly.

Density is typically found to exhibit a pronounced boron anomaly effect [33], which is also observed in the present experiments and simulations (Fig. 4). A significant deviation between simulation and experimental data is observed for the MD0 glass, likely due to the inability of the potential to describe the MRO as discussed above for the structure factor. Besides this deviation, the simulations reproduce the boron anomaly effect in density, with a maximum at a Li_2O concentration of ∼40 mol%. There is, however, a minor difference (∼ 5%) in the absolute density values for this composition. Furthermore, the simulated density decreases more rapidly than the experimental density at modifier concentrations above the maximum density. For the present experimental glasses, we observe good agreement with previously reported experimental density values in Fig. 4 [33].

In summary, the utilized potential captures the main structural features in the lithium borate glasses, especially at low Li_2O concentrations as probed by the Wright R_χ factor. At higher concentrations of Li_2O, deviation is observed both in the SRO and MRO. In the SRO, this is mainly caused by some deviation in peak positions as shown by the $g_N(r)$. While the R_χ factor is not low (<9%) for high concentrations of Li_2O, the potential accurately captures the composition dependence of density and N_4. As free volume and network connectivity are expected to be two of the most important factors for the thermal conductivity, we continue using the potential to understand heat propagation in the present glasses.

B. Thermal conductivity

Figure 5 presents the thermal conductivity as a function of lithium modifier content for both the experimental and simulated glasses (note the different scale on the two vertical axes). Data for the latter have been obtained from equilibrium molecular dynamics simulations using the GK approach. First, we find excellent agreement between the present experimental κ value for pure B_2O_3 and that of a previous experimental study [54]. For the present experimental glasses, we observe a clear boron anomaly in κ. The thermal conductivity increases linearly with increasing Li_2O content below ∼35 mol%, then reaches a maximum plateau, and finally decreases for the Li48 glass. This trend in κ is similar to that previously observed for other alkali (Na, K) borates in the molten state [27,28]. While the thermal conductivity shows a clear boron anomaly, the thermal diffusivity (α) exhibits an even more pronounced nonlineraity with a clear maximum of α at around 30 mol% Li_2O (Fig. S5 in the Supplemental Material [38]).

The simulated glasses exhibit the same qualitative trend in conductivity as the experimental glasses, thus first showing an increase in thermal conductivity up to a maximum value in the range of 30–35 mol% Li_2O, followed by a decrease in κ for higher lithium content (Fig. 5). The absolute values of κ for the simulated glasses are, however, systematically larger than those of the experimental glasses by a factor of 3 to 5. This is commonly observed in MD simulations of thermal conductivity and has previously been ascribed to the incorporation of full occupation of the VDOS in MD simulations, even below the Debye temperature [12,36].

Understanding the correlations between various physical properties and structural features of glassy systems is important for enabling rational design of new compositions [55]. For borates, the composition dependence of various properties, such as density and hardness, is largely controlled by the change in N_4 [33,56]. Here, we present a plot of experimental thermal conductivity against N_4 values (obtained from Ref. [25]) in Fig. 6. A strong linear correlation between N_4 and κ is observed, in agreement with the findings of Kim and Morita [27,28] for other alkali borates in the molten state, but, unlike the present study, with data for only three compositions for each modifier. A plot of simulated κ vs N_4 also shows a linear correlation, although the error bars are larger (Fig. S6 in the Supplemental Material [38]). We also find an approximate linear correlation between thermal

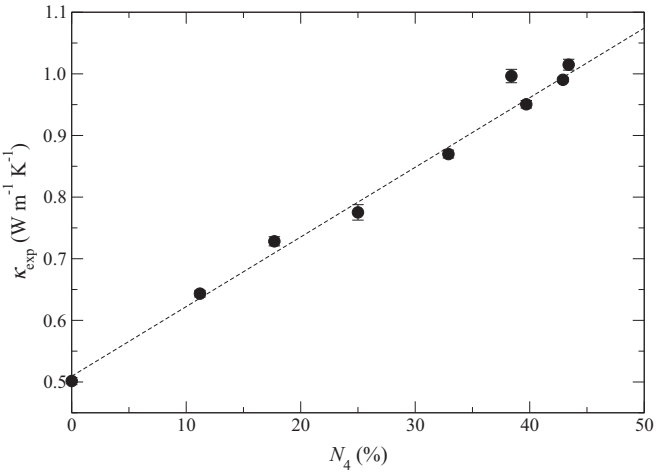

FIG. 6. Dependence of the experimental thermal conductivity (κ_{exp}) on the fraction of fourfold coordinated to total boron (N_4) for the whole range of studied lithium borate glasses. Values of N_4 are from Ref. [25]. The dashed line is a guide for the eye.

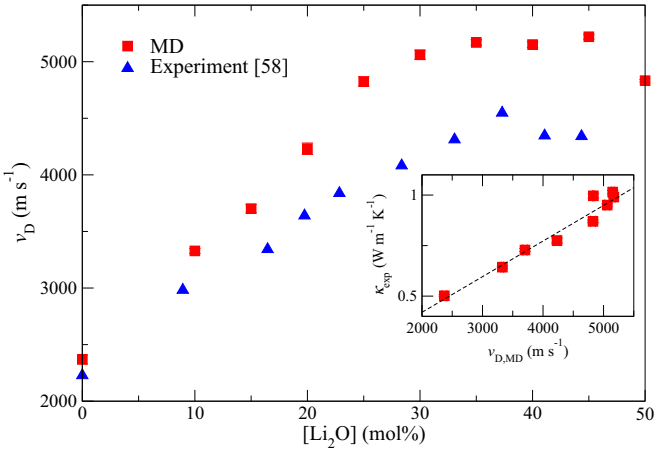

FIG. 7. Debye sound velocities (v_D) obtained from simulations at 0 K [calculated using Eq. (13)] and experimental data (from Ref. [58]) plotted as a function of Li_2O content. Inset: correlation between the Debye sound velocities from MD and the experimental thermal conductivities (κ_{exp}) where the Debye sound velocity of the MD50 glass is plotted against the κ_{exp} of the Li48 glass. The dashed line is a guide for the eye.

diffusitivity and the absolute concentrations of B^4 units (Fig. S7 in the Supplemental Material [38]). The qualitative agreement between experiments and MD simulations suggest that the utilized potential can be applied to predict compositional trends in the thermal conductivity of borate-based glasses. In future work, it would also be interesting to further test the relationship between thermal conductivity and boron speciation, which could be done by testing the thermal and pressure history dependence of thermal conductivity and extending the studies to borosilicate glasses.

C. Phonon gas model

To understand the N_4-κ correlation, we here consider the PGM of thermal conductivity [5,6],

$$\kappa = \tfrac{1}{3} c v_D l_{MFP}, \tag{12}$$

where c is the phonon volumetric heat capacitiy, v_D is the phonon velocity (commonly taken as the velocity of sound or the Debye sound velocity, v_D [11]), and l_{MFP} is the phonon mean free path (MFP). In this study, we use v_D as it holds contributions from both longitudinal and transversal modes. v_D is calculated as,

$$v_D = \sqrt[-3]{\frac{1}{3}\left(\frac{1}{v_L^3} + \frac{2}{v_T^3}\right)}, \tag{13}$$

where v_L and v_T are the longitudinal and transversal sound velocities, respectively [57]. PGM assumes all modes to be propagating with scattering events usually occurring every distance of the l_{MFP}, which is generally agreed not to be the case in amorphous systems [7,10,11]. However, we consider it here, as it provides an intuitive approach for correlating changes in thermal conductivity with structural changes. Considering the parameters in Eq. (12), we first note that the measured heat capacity of the system is found to monotonically increase with increasing amount of Li_2O (Table I). Converting the measured isobaric heat capacity into volumetric units by multiplying with the density, we observe an overall increase in the studied composition range (Fig. S8 in the Supplemental Material [38]). This observed change in c should contribute to some of the observed increase in κ for low Li_2O contents.

Next, we consider the phonon velocities, which can be challenging to analyze due to their frequency dependency. Lorösch *et al.* have shown that the transversal and longitudinal sound velocities approximately double when comparing pure B_2O_3 to a $44Li_2O$-$66B_2O_3$ glass [58]. Above 44 mol% Li_2O, a plateau in the longitudinal velocity and a slight decrease in the transverse velocity are observed. Even though this trend may not apply to all modes, the increase of both longitudinal and transversal sound velocities is likely related to the increase of κ as noted by both the PGM and models involving diffusive modes [6,59,60]. Figure S9 in the Supplemental Material presents an approximate linear correlation between the measured thermal conductivity and the Debye sound velocity of the acoustic phonons in the range of 0–40 mol% Li_2O [38]. To circumvent the problem of lacking sound velocity data above 40 mol% Li_2O [58], we estimate the sound velocities for the entire range of compositions by determining the C_{11} and C_{44} elastic constants at 0 K using the MD simulations (see Sec. III D) and compare them with the experimental literature data (Fig. 7). The experimental and simulated data exhibit the same compositional trend, but the absolute values of sound velocity for the simulated glasses are generally 15–30% larger than the experimental ones at room temperature. We note that the Debye sound velocity of the MD50 glass is lower than that of the glasses with lower lithium content, which could help to explain the observed decrease in thermal conductivity in this composition range (Fig. 5). The inset of Fig. 7 shows the experimental thermal conductivity plotted against the simulated Debye sound velocities. A positive correlation is observed, but again with some deviation from linearity in the range of 25–35 mol% Li_2O. Interestingly, we note that Lorösch *et al.* found a similar compositional trend in sound velocities for other alkali borates, yet with smaller absolute changes [58].

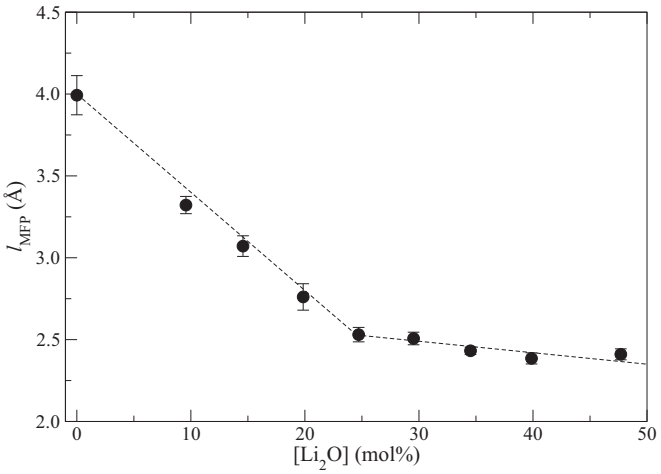

FIG. 8. Composition dependence of the phonon mean free path (l_{MFP}) as estimated from the experimental C_p, density, and thermal conductivity while the used Debye sound velocities are from MD simulations The dashed line is a guide for the eye.

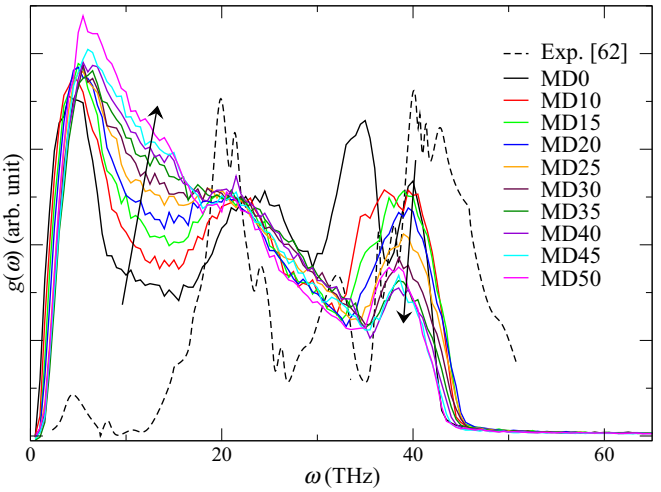

FIG. 9. Total vibrational density of states $g(\omega)$ presented for all MD simulated compositions as well as experimental data of pure vitreous B_2O_3 (correspoinding to MD0) from inelastic neutron scattering Ref. [62]. Arrows indicate trends in the $g(\omega)$ intensity with increasing Li_2O concentration.

This supports the universality of the present findings, at least within the alkali borate family.

Finally, we also consider the effect of l_{MFP} on the thermal conductivity in the studied glasses. By combining the measured thermal conductivities, densities, heat capacities, and simulated Debye sound velocities, we can estimate the l_{MFP} in the studied glass series using Eq. (12). Even though this will not give correct absolute values of l_{MFP} due to the reasons discussed above, the compositional trend in l_{MFP} should be valid. As shown in Fig. 8, the estimated l_{MFP} rapidly decreases with increasing lithium content in the range of 0–25 mol% Li_2O, followed by a change in slope and thus a significantly smaller decrease in l_{MFP} for higher lithium contents. The small decrease in l_{MFP} above 25 mol% Li_2O might be because the value of l_{MFP} approaches the length of the smallest interatomic spacing in the network (the B-O bond). For example, l_{MFP} for the Li40 glass calculated using only experimental values is 2.7 Å, which compares to the experimental interatomic spacing of ∼1.4 Å for the B-O bond as found in the experimental $g_N(r)$ of a $33Li_2O$-$67B_2O_3$ glass [39] (see Fig. S4 in the Supplemental Material [38]). The observation that l_{MFP} is on the same order as the interatomic spacings suggests that the heat may not be transferred by propagating modes, but by diffusive modes, so-called diffusons [7,10,13]. Similar arguments for a lower limit of l_{MFP} have previously been discussed by Kittel [6] and Clarke [61].

D. Vibrational density of states

To study the vibrational characteristics and its relation to the thermal conductivity, we calculate the VDOS in the simulated glasses (see Sec. III E). Figure 9 shows the simulated VDOS of pure B_2O_3 along with experimental data [62]. Pronounced discrepancies are noted in the low frequency range, especially in intensity, while at higher frequencies the potential captures the modal character of borate glass relatively well, with an overall replication of the three main experimental peaks. An earlier study [63] reported higher intensity at lower frequencies and lower intensities in the high frequency area compared to that in Ref. [62]. We have not been able to find experimental VDOS data in the literature for lithium borate glasses. As the VDOS is generally very challenging to replicate in MD simulations, even when the potential replicates the structure accurately [37,64], we here only use the VDOS to make relative comparisons within the series.

Figure 9 shows the total VDOS for all simulated glasses. All modes lie in the range of 0–45 THz, but with increasing Li_2O concentration, an increasing amount of modes appear in the low-frequency region (5–20 THz). In addition, two major peaks of the MD0 glass at ∼34 and 40 THz first decrease in intensity and then apparently merge into a single peak at ∼38 THz for Li_2O concentrations above 25 mol%. On the other hand, the frequency range from 20–30 THz is largely unaffected by the addition of Li_2O. Next, we consider the partial VDOS for Li, B, and O (Fig. 10). For lithium, the VDOS is seen to increase monotonically in intensity with increasing Li_2O concentration in the low frequency region, with a dominant peak at ∼8 THz. For boron, there is an overall decrease of occupation of all modes across the spectral range except for the peak at ∼38 THz. The occupation of this mode initially decreases with increasing lithium content, until it increases in occupation for the MD50 glass. A similar effect is also observed for the low-frequency part of the oxygen partial VDOS.

The nonmonotonic variations in the VDOS of B and O is likely related to the similar nonmonotonic variation in the boron coordination number change, thus κ. This could suggest that the ionocovalent network is the major source of heat transfer in the system. Following earlier work, an alternative interpretation would be to consider overlapping modes in the VDOS as the general source of heat transfer [65,66]. Considering the present partial VDOS in Fig. 10, the overlaps of Li and O modes at low frequencies as well as B

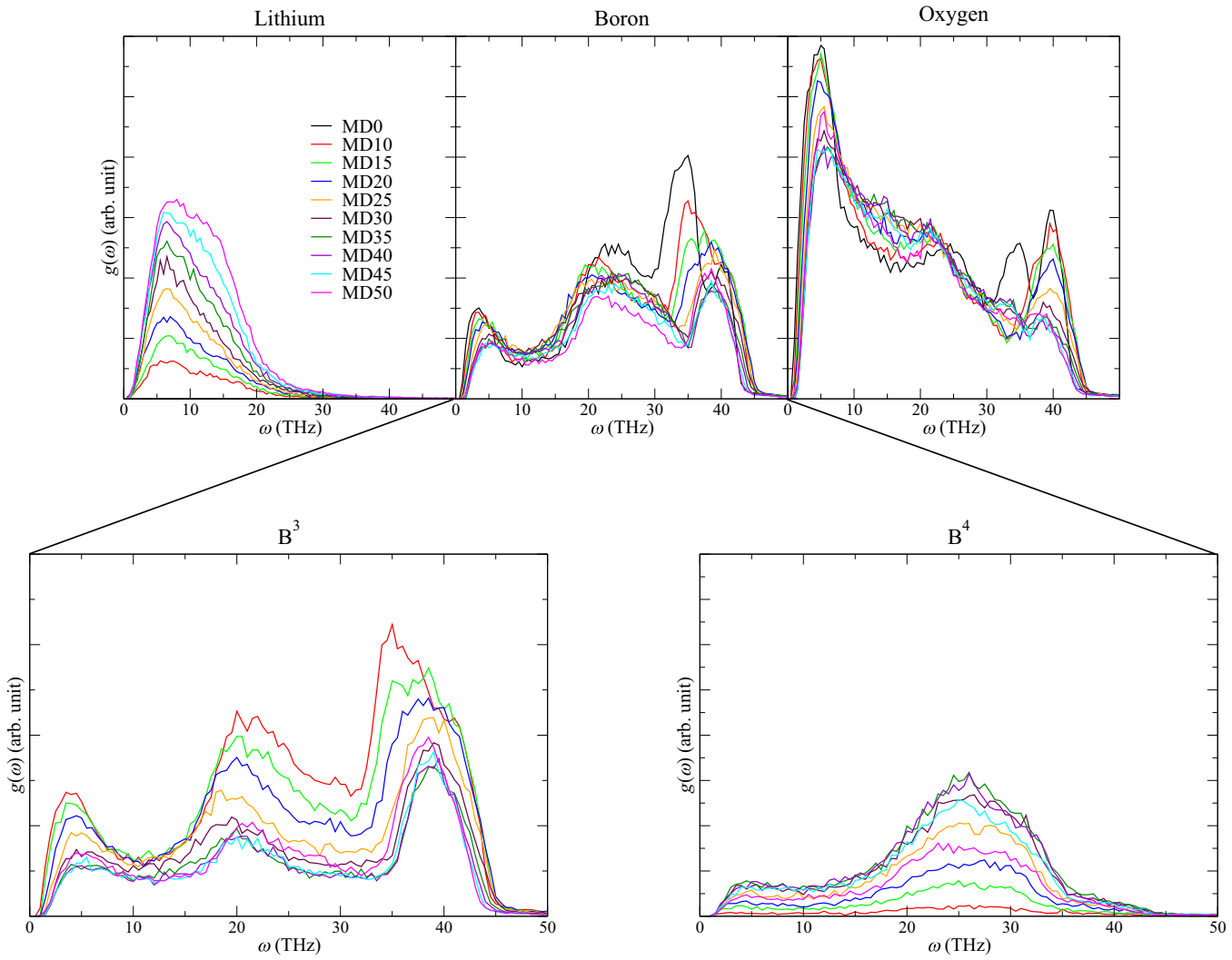

FIG. 10. Partial vibrational density of states $g(\omega)$ as calculated from MD for the three components (Li, B, O) of the studied lithium borate glasses. The partial VDOS is boron is further deconvoluted into contributions from three- and fourfold coordinated states. Notice that the vertical axes in each row have the same scale for the ease of comparison.

and O overlaps at higher frequencies could also be causing the observed trend of κ. The latter interpretation would also naturally account for differences in κ of binary borate systems with different modifiers, as it has been observed in the molten state [27,28], thus explicitly having contributions to κ from all types of atoms in the glass. To further investigate the partial VDOS of boron, we have calculated the VDOS of B^3 and B^4 species, respectively (Fig. 10). The modes of B^3 exist in the whole frequency range, while those of B^4 primarily occur around 20–30 THz. A monotonic decrease in the intensity of B^3 modes is noted with increasing Li_2O content, while the B^4 modes feature a clear anomalous effect with the strongest bands present for the MD35 and MD40 glasses.

To study the contribution of the modes to the measured thermal conductivity, we calculate the Fourier transform of the HCACF (Fig. 11), following earlier work [47,48]. The most significant heat current carrying modes are present at 25 and 35 THz for the MD0 glass, and these two bands become broader and decrease in intensity with increasing fraction of Li_2O. The observed changes in frequencies correspond well with the relative changes in the partial VDOS of B^3 and B^4 (Fig. 10), supporting the notion that the borate network is an important contributor to the heat conduction. In Fig. 11, we also note the occurrence of a band at 5–10 THz when lithium is introduced, and thus lithium is also believed to contribute to the heat conduction, as suggested from the partial VDOS. Moreover, there are large differences in intensity between the low and high frequency bands in Fig. 11, with the intensity of the Fourier transform being related to the amplitude of the modes in the HCACF. As a number of modes contribute negatively to the HCACF (see Fig. S3 of the Supplemental Material [38]), the intensities of the bands in Fig. 11 cannot be directly correlated to a change in κ, but only seen as contributions to the HCACF.

Finally, we discuss the calculated VDOS in relation to earlier work on modal character. Allen and Feldman provided a thorough description of the diffusive character of some modes in amorphous systems [7,9,10]. Generally a gradual transition from propagating to diffusive character, termed the

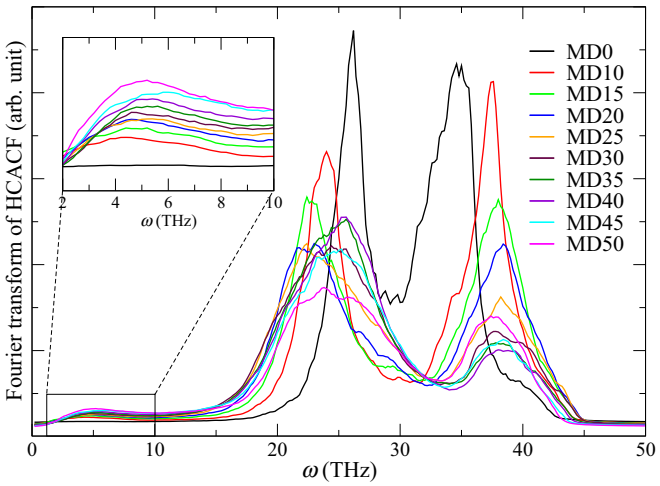

FIG. 11. Fourier transforms of the heat current autocorrelation function (HCACF) of each simulated glass, as calculated using Eq. (11). Inset: zoom of the low frequency regions. The curves represent the average of Fourier transforms of ten HCACFs.

Ioffe-Regel crossover, has been found in several amorphous materials from MD simulations. For amorphous Si, the crossover has been observed at ∼3 THz [7], with an even lower crossover value for amorphous SiO_2 [67]. Experimental data also report crossover values in this range for amorphous Si [68,69]. In this work, the vast majority of the vibrational modes are found at significantly higher frequencies. Moreover, we find a very short MFP in the range of intermolecular distances. As such, the majority of the modes in the simulated lithium borate glasses should be diffusive rather than propagating. This is consistent with results for other amorphous materials, although a more thorough analysis is required to confirm this, which is beyond the scope of the current work.

V. SUMMARY AND CONCLUSIONS

The thermal conductivity of a series of binary lithium borate glasses has been determined both experimentally and using MD simulations. A clear boron anomaly effect has been found with a maximum in thermal conductivity at around 35–40 mol% Li_2O for both measurements and simulations, even though the simulations overestimate the thermal conductivity by a factor of 3–5. This variation in thermal conductivity is correlated linearly with that in the fraction of fourfold coordinated boron and the Debye sound velocity of the glasses. Based on the phonon gas model, we suggest that the variation in phonon velocities is the main structural origin of the boron anomaly effect in thermal conductivity. We also estimated the variation in the phonon MFP by combining experimental and simulated results, showing an overall decrease with modifier content and the convergence of the MFP with the interatomic spacings in the network. This suggests the primary character of the modes to be diffusive rather than propagating. By combining experimental and molecular dynamics results we ultimately suggest that heat is conducted through both the covalent as well as the modifier network, yet we believe the increase of the boron coordination number is of significant importance to the increase of the sound velocity, and hence the found increase of thermal conductivity. This connection provides a link between structural changes and thermal conductivity that may be extendable to a wider range of oxide glasses.

ACKNOWLEDGMENTS

We thank L. J. Liermann and Y. Lin (Penn State University) for help with the ICP-OES measurements, and C. Steinmann (Aalborg University) and K.-H. Lee (Penn State University) for helpful discussions on the MD simulations. Computational resources were provided by the DeIC National HPC Center (ABACUS 2.0) at the University of Southern Denmark and funded by Aalborg University.

[1] J. C. Mauro, C. S. Philip, D. J. Vaughn, and M. S. Pambianchi, Int. J. Appl. Glas. Sci. **5**, 1 (2014).
[2] M. C. Wingert, J. Zheng, S. Kwon, and R. Chen, Semicond. Sci. Technol. **31**, 113003 (2016).
[3] E. H. Ratcliffe, Glas. Technol. **4**, 113 (1963).
[4] M. K. Choudhary and R. M. Potter, in *Properties of Glass-Forming Melts*, edited by L. D. Pye, A. Montenero, and I. Joseph (CRC, Boca Raton, FL, 2005).
[5] R. Peierls, Ann. Phys. **395**, 1055 (1929).
[6] C. Kittel, Phys. Rev. **75**, 972 (1949).
[7] P. B. Allen, J. L. Feldman, J. Fabian, and F. Wooten, Philos. Mag. B **79**, 1715 (1999).
[8] W. Lv and A. Henry, Sci. Rep. **6**, 37675 (2016).
[9] P. B. Allen and J. L. Feldman, Phys. Rev. Lett **62**, 645 (1989).
[10] P. B. Allen and J. L. Feldman, Phys. Rev. B **48**, 12581 (1993).
[11] R. C. Zeller and R. O. Pohl, Phys. Rev. B **4**, 2029 (1971).
[12] W. Lv and A. Henry, Sci. Rep. **6**, 35720 (2016).
[13] J. L. Feldman, M. D. Kluge, B. Allen, and F. Wooten, Phys. Rev. B **48**, 12589 (1993).
[14] W. Schirmacher, Europhys. Lett. **73**, 892 (2006).
[15] V. Lubchenko and P. G. Wolynes, Proc. Natl. Acad. Sci. **100**, 1515 (2003).
[16] H. Ohta, H. Shibata, H. Hasegawa, T. Kowatari, Y. Shiroki, S.-Y. Kitamura, and Y. Waseda, J. Manuf. Sci. Prod. **13**, 115 (2013).
[17] H. Shibata, A. Suzuki, and H. Ohta, Mater. Trans. **46**, 1877 (2005).
[18] M. M. Ammar, S. A. Gharib, M. M. Halawa, H. A. El-Batal, and K. El-Badry, Commun. Am. Ceram. Soc. **66**, C-76 (1983).
[19] N. A. Ghoneim and M. M. Halawa, Thermochim. Acta **83**, 341 (1985).
[20] M. M. Ammar, M. M. Halawa, N. A. Ghoneim, A. F. Abbas, and H. A. El Batal, J. Am. Ceram. Soc. **65**, c174 (1982).
[21] P. F. van Velden, Glas. Technol. **6**, 166 (1965).
[22] N. A. Ghoneim, H. A. El Batal, and K. El-Badry, Glas. Berichte **56**, 934 (1983).
[23] M. M. Smedskjaer, J. C. Mauro, R. E. Youngman, C. L. Hogue, M. Potuzak, and Y. Yue, J. Phys. Chem. B **115**, 12930 (2011).

[24] R. E. Youngman, S. T. Haubrich, J. W. Zwanziger, M. T. Janicke, and B. F. Chmelka, Science **269**, 1416 (1995).
[25] S. A. Feller, W. J. Dell, and P. J. Bray, J. Non. Cryst. Solids **51**, 21 (1982).
[26] Y. Kim, Y. Yanaba, and K. Morita, J. Non. Cryst. Solids **415**, 1 (2015).
[27] Y. Kim and K. Morita, J. Am. Ceram. Soc. **98**, 1588 (2015).
[28] Y. Kim and K. Morita, J. Am. Ceram. Soc. **98**, 3996 (2015).
[29] M. Tohmori, T. Sugawara, S. Yoshida, and J. Matsuoka, Phys. Chem. Glasses: Eur. J. Glass Sci. Technol. B **50**, 358 (2009).
[30] M. K. Bødker, J. C. Mauro, R. E. Youngman, and M. M. Smedskjaer, J. Phys. Chem. B **123**, 1206 (2019).
[31] G. D. Chryssikos, J. A. Duffy, J. M. Hutchinson, M. D. Ingram, E. I. Kamitsos, and A. J. Pappin, J. Non. Cryst. Solids **172-174**, 378 (1994).
[32] J. C. Mauro, P. K. Gupta, and R. J. Loucks, J. Chem. Phys. **130**, 234503 (2009).
[33] M. Shibata, C. Sanchez, H. Patel, S. Feller, J. Stark, G. Sumcad, and J. Kasper, J. Non. Cryst. Solids **85**, 29 (1986).
[34] L. Deng and J. Du, J. Am. Ceram. Soc. **102**, 2482 (2019).
[35] M. Wang, N. M. Anoop Krishnan, B. Wang, M. M. Smedskjaer, J. C. Mauro, and M. Bauchy, J. Non. Cryst. Solids **498**, 294 (2018).
[36] P. Jund and R. Jullien, Phys. Rev. B **59**, 13707 (1999).
[37] Y. Tian, J. Du, W. Han, X. Zu, X. Yuan, and W. Zheng, J. Chem. Phys. **146**, 054504 (2017).
[38] See Supplemental Material at http://link.aps.org/supplemental/10.1103/PhysRevMaterials.3.075601 for further details about thermal, structural, and elastic properties of the simulated glasses as well as XRD spectra and an example plot of the performed Maier-Kelley fitting.
[39] Y. Z. Yue, J. Non. Cryst. Solids **354**, 1112 (2008).
[40] C. G. Maier and K. K. Kelley, J. Am. Chem. Soc. **54**, 3243 (1932).
[41] S. Plimpton, J. Comput. Phys. **117**, 1 (1995).
[42] J. Swenson, L. Börjesson, and W. S. Howells, Phys. Rev. B **52**, 9310 (1995).
[43] D. P. Sellan, E. S. Landry, J. E. Turney, A. J. H. McGaughey, and C. H. Amon, Phys. Rev. B **81**, 214305 (2010).
[44] A. J. H. McGaughey and J. M. Larkin, Annu. Rev. Heat Transf. **17**, 49 (2014).
[45] Z. Wang, S. Safarkhani, G. Lin, and X. Ruan, Int. J. Heat Mass Transf. **112**, 267 (2017).
[46] C. Kittel, *Introduction to Solid State Physics*, 8th ed. (Wiley, New York, 2005).
[47] E. S. Landry, M. I. Hussein, and A. J. H. McGaughey, Phys. Rev. B **77**, 184302 (2008).
[48] M. J. Abdolhosseini Qomi, F.-J. Ulm, and R. J.-M. Pellenq, Phys. Rev. Appl. **3**, 064010 (2015).
[49] S. Le Roux and P. Jund, Comput. Mater. Sci. **49**, 70 (2010).
[50] R. A. Barrio, R. Kerner, M. Micoulaut, and G. G. Naumis, J. Phys. Condens. Matter **9**, 9219 (1997).
[51] A. C. Wright, J. Non. Cryst. Solids **159**, 264 (1993).
[52] D. R. Uhlmann and R. R. Shaw, J. Non. Cryst. Solids **1**, 347 (1969).
[53] W. J. Dell, P. J. Bray, and S. Z. Xiao, J. Non. Cryst. Solids **58**, 1 (1983).
[54] O. Nilsson, O. Sandberg, and G. Bäckström, Int. J. Thermophys. **6**, 267 (1985).
[55] J. C. Mauro, A. Tandia, K. D. Vargheese, Y. Z. Mauro, and M. M. Smedskjaer, Chem. Mater. **28**, 4267 (2016).
[56] M. M. Smedskjaer, J. C. Mauro, and Y. Yue, Phys. Rev. Lett. **105**, 115503 (2010).
[57] A. K. Varshneya, *Fundamentals of Inorganic Glasses* (Academic, New York, 2013).
[58] J. Lorösch, M. Couzi, J. Pelous, R. Vacher, and A. Levasseur, J. Non. Cryst. Solids **69**, 1 (1984).
[59] M. T. Agne, R. Hanus, and G. J. Snyder, Energy Environ. Sci. **11**, 609 (2018).
[60] D. G. Cahill, S. K. Watson, and R. O. Pohl, Phys. Rev. B **46**, 6131 (1992).
[61] D. R. Clarke, Surf. Coatings Technol. **163-164**, 67 (2003).
[62] R. N. Sinclair, R. Haworth, A. C. Wright, B. G. Parkinson, D. Holland, J. W. Taylor, N. M. Vedishcheva, I. G. Polyakova, B. A. Shakhmatkin, S. A. Feller, B. Rijal, and T. Edwards, Phys. Chem. Glasses: Eur. J. Glass Sci. Technol. B **47**, 405 (2006).
[63] A. C. Hannon, R. N. Sinclair, J. A. Blackman, A. C. Wright, and F. L. Galeener, J. Non. Cryst. Solids **106**, 116 (1988).
[64] M. Bauchy, J. Chem. Phys. **141**, 024507 (2014).
[65] E. T. Swartz and R. O. Pohl, Rev. Mod. Phys. **61**, 605 (1989).
[66] X. Zhang and J. Jiang, J. Phys. Chem. C **117**, 18441 (2013).
[67] H. R. Seyf and A. Henry, J. Appl. Phys. **120**, 025101 (2016).
[68] J. L. Braun, C. H. Baker, A. Giri, M. Elahi, K. Artyushkova, T. E. Beechem, P. M. Norris, Z. C. Leseman, J. T. Gaskins, and P. E. Hopkins, Phys. Rev. B **93**, 140201 (2016).
[69] J. M. Larkin and A. J. H. McGaughey, Phys. Rev. B **89**, 144303 (2014).